Current Biology, Volume *30*

Supplemental Information

Dynamic Signal Compression for Robust Motion Vision in Flies

Michael S. Drews, Aljoscha Leonhardt, Nadezhda Pirogova, Florian G. Richter, Anna Schuetzenberger, Lukas Braun, Etienne Serbe, and Alexander Borst

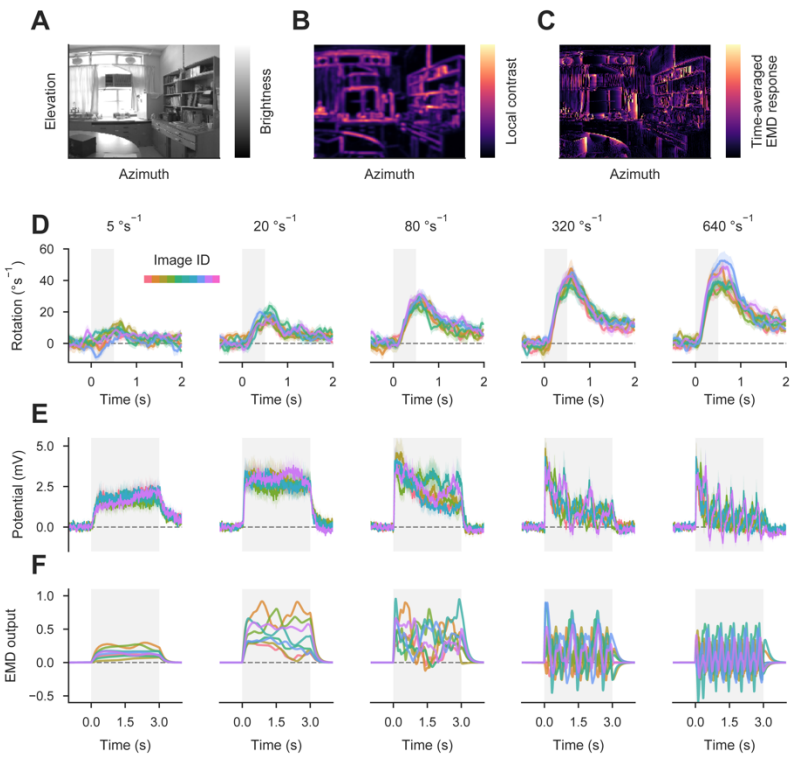

Figure S1 | Behavioral, neural, and model responses to natural scenes. Related to Figure 1. (**A**) Natural image patch as seen through the field of view of model LPTC. (**B**) Estimate of local contrast in natural image patch. RMS contrast was estimated by filtering the image with a Gaussian ($\sigma = 0.5$ º), subtracting the filtered image from the original, squaring the mean-subtracted image, filtering it with a Gaussian ($\sigma = 0.5$ º), and taking the square root. (**C**) Spatially reconstructed output of simulated LPTC for same image patch as before, plotted as the square root of the time-averaged response. A horizontally motion-sensitive LPTC was constructed using the same parameters as in Figure 1F (STAR Methods) with the exception of more fine-grained sampling at exactly the image resolution. The depicted panorama was moved for 16 s at a velocity of 22.5 ºs^{-1}, resulting in a single complete rotation. Responses at each pixel location were then averaged across the full stimulus period. This demonstrates that the response of the EMD array depends strongly on squared local image contrast. (**D**) Turning responses for 8 images (indicated by trace color) and 5 velocities (indicated by panel title; N=16 wild-type flies; data as in Figure 1B). Gray shaded area indicates duration of motion stimulus. (**E**) Membrane potential for 6 images and 5 velocities (N=11 HS cells from 9 flies; data as in Figure 1D). (**F**) Output of model LPTC for same images and velocities as E (data as in Figure 1F). See Table S2.

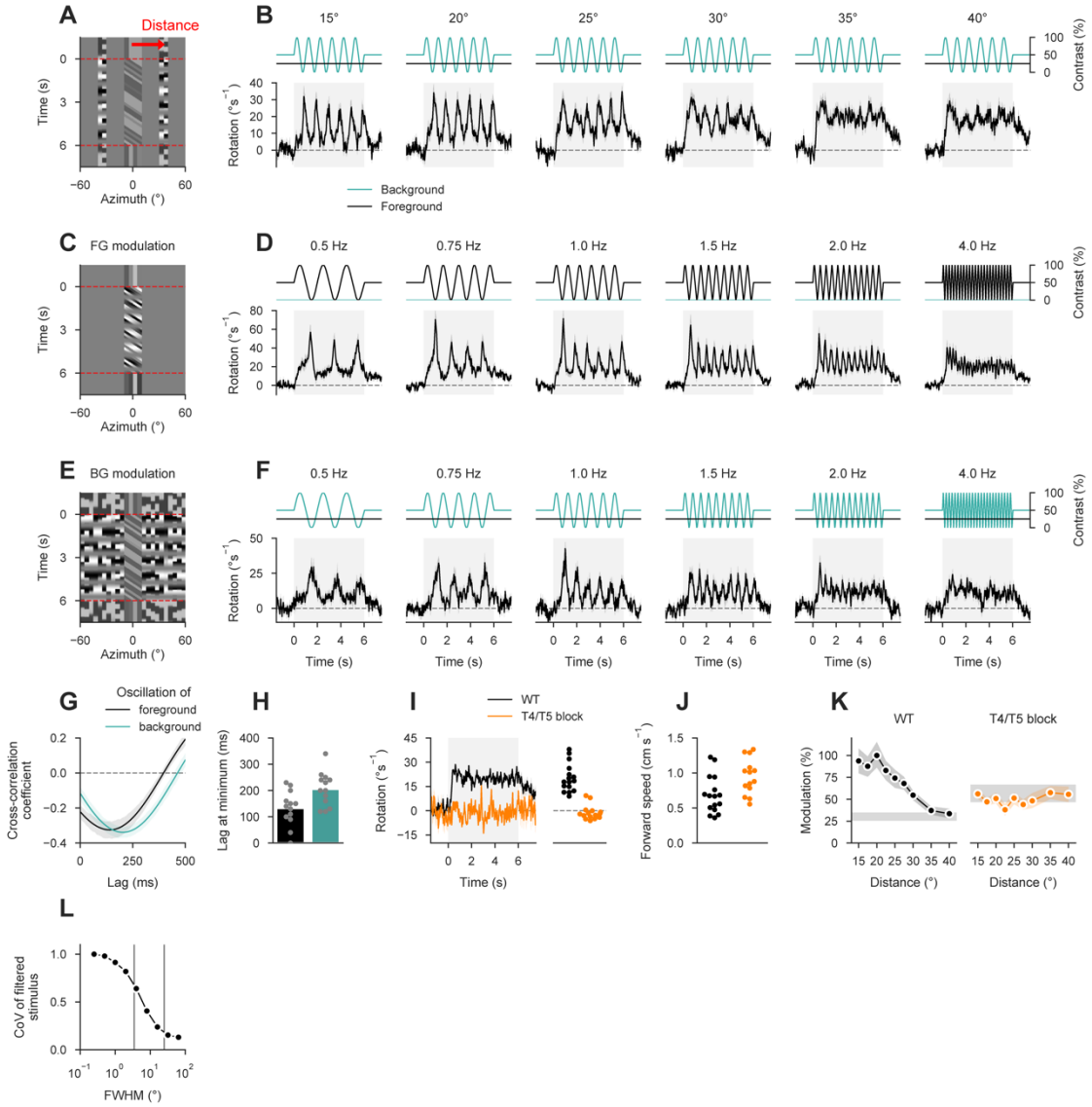

Figure S2 | Detailed behavioral responses to contrast stimuli. Related to Figure 2.
(**A**) Illustration of spatial oscillation experiment. Background was restricted to 10 º wide stripes flanking the foreground motion stimulus at the center distance indicated by the red arrow. Dashed lines indicate period during which foreground pattern moved at 50 ºs^{-1}. This arrangement was repeated at plus and minus 90 º from the frontal axis of the fly; 0 º in this plot indicates the center of the foreground. (**B**) Contrast traces and turning responses for five distance conditions (indicated above each panel). Top, instantaneous contrast (25 % in foreground, oscillating at 1 Hz in background). Bottom, turning response of the fly (N=16 wild-type flies). Modulation was reduced as spacing between foreground and background increased. (**C**) Illustration of temporal foreground modulation stimulus at 1 Hz frequency. (**D**) Contrast traces and turning responses for five foreground oscillation frequencies (N=13; background contrast was 0 %). Modulation decreased as frequency increased. (**E**) Illustration of temporal background modulation stimulus at 1 Hz frequency. (**F**) Contrast traces and turning responses for five background oscillation frequencies (N=13; foreground contrast was 25 %). Modulation again decreased with frequency. (**G**) Normalized cross-correlation between contrast oscillation and turning behavior for 1 Hz data from D and F. (**H**) Lag between stimulus oscillation and turning, evaluated as per-fly lag at first minimum within 500 ms for cross-correlations from G. (**I**) Left, comparison of turning responses between wild-type flies and flies in which T4/T5 cells were silenced using TNT (STAR Methods; N=16/14 for WT/block flies). Right, turning responses averaged between 0 and 6 s following motion onset. Syndirectional turning was abolished in T4/T5-silenced flies. (**J**) Average forward speed throughout full experiment. T4/T5 block flies did not exhibit

locomotion deficiencies. (**K**) Comparison of spatial oscillation tuning. T4/T5 block flies did not show modulation at the contrast oscillation frequency of 1 Hz and a generally increased level of baseline fluctuation. (**L**) Evaluation of luminance properties at different spatial scales for the behavioral stimulus. Normalized coefficient of variation across visual field was calculated after applying a Gaussian filter with different full-widths at half-maximum (FWHM). Gray lines indicate typical FWHM of ommatidium (left) and full receptive field of medulla cells (right). See Table S2.

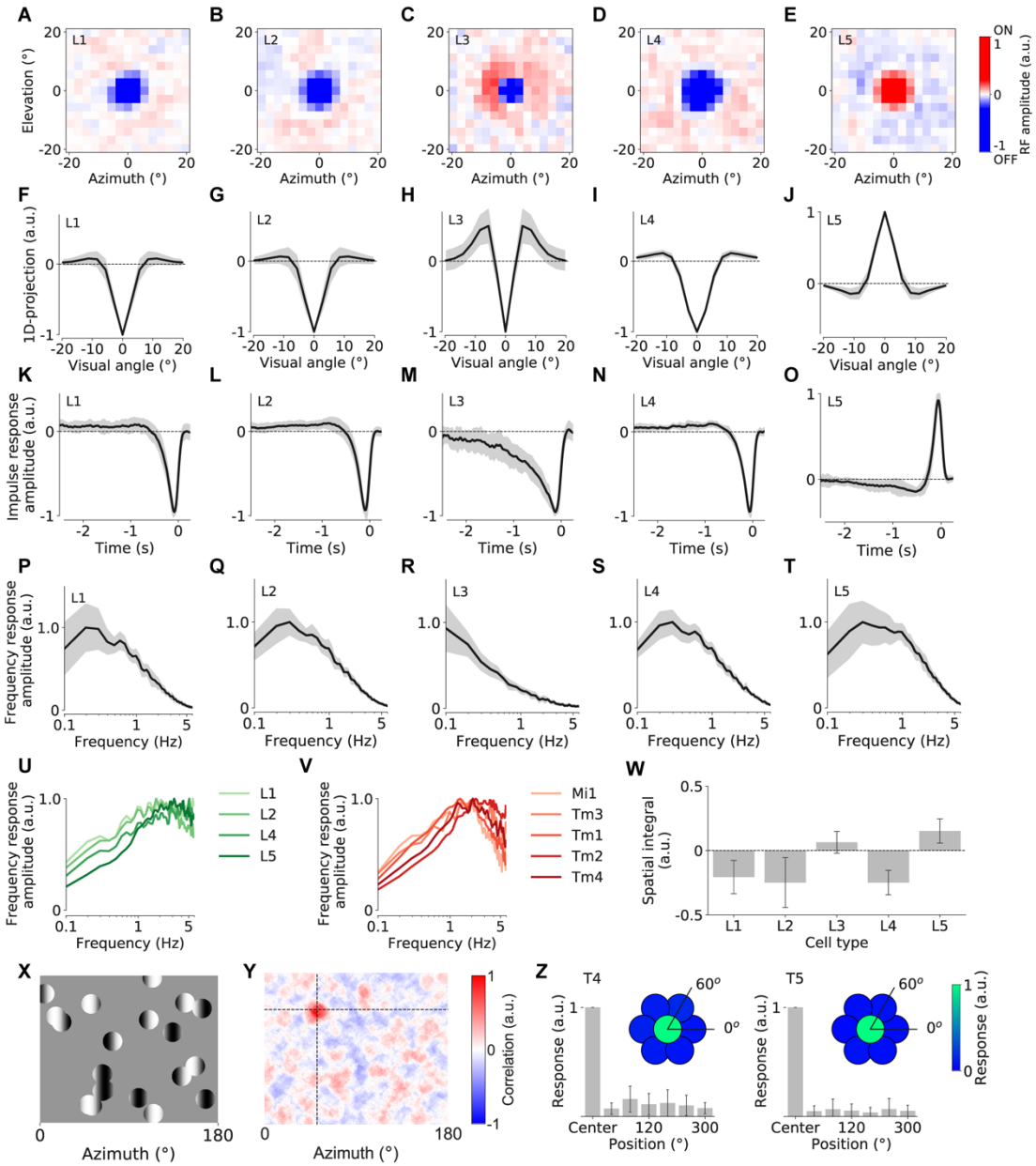

Figure S3 | Lamina and T4/T5 receptive field mapping. Related to Figure 3.
(**A–E**) Averaged 2D spatial receptive fields (RF) of L1–L5 from reverse correlation using white noise stimulation (L1: 21/7 cells/flies, L2: 34/5, L3: 34/5, L4: 17/6, L5: 18/9). (**F–J**) 1D projection (averaged over all orientations) of the RFs in A–E. All cell types possessed linear RFs with antagonistic center-surround structure. (**K–O**) Temporal RFs measured in the center of the spatial RFs. (**P–T**) Frequency-space representations of temporal RFs. (**U**) Frequency representations of lamina transient cells (all lamina cells except for L3) after deconvolution with a putative linear GCaMP6f low-pass filter with time constant 350 ms as performed previously [S1]. (**V**) Deconvolved frequency responses of medulla bandpass filter cells (replotted from previous work [S1]). (**W**) Spatial integral of the 2D RFs in A–E. For L3, the strong antagonistic ON surround exactly counterbalanced the OFF-center contribution. (**X**) x-y plot of the stochastic motion noise stimulus used for localizing T4/T5 RFs. (**Y**) Example RF of a T4 cell from reverse correlation with the motion noise stimulus. (**Z**) Average responses of T4/T5 to 25 ° windowed drifting gratings probing different positions around the estimated RF center. This validated the RF coordinates obtained from the stochastic motion noise stimulus. All data are shown as mean ± s.d. See Table S2.

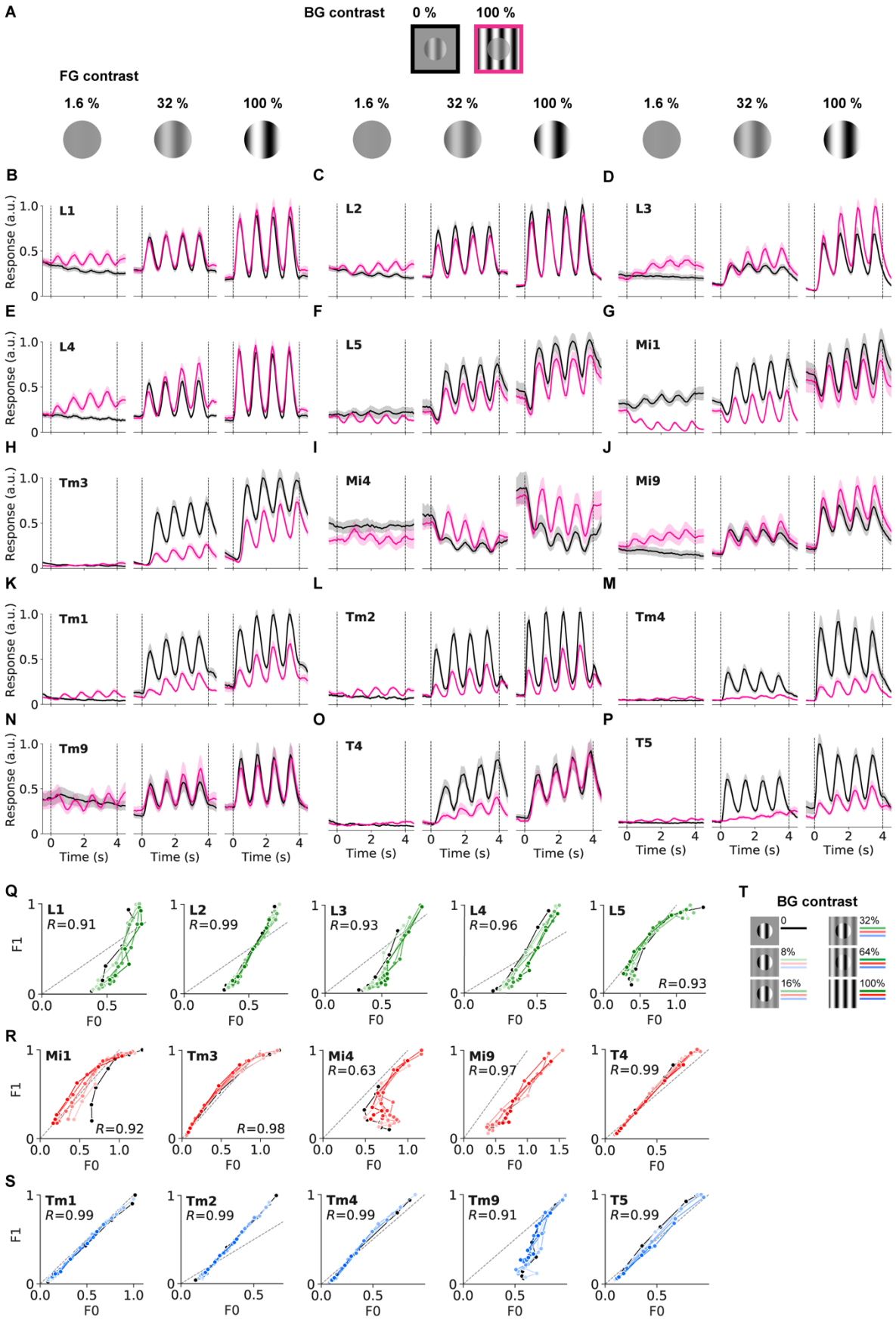
A
BG contrast
0 %
100 %
FG contrast
1.6 %
32 %
100 %
B
C
D
E
F
G
H
I
J
K
L
M
N
O
P
Q
R
S
T
L1
L2
L3
L4
L5
Mi1
Tm3
Mi4
Mi9
Tm1
Tm2
Tm4
Tm9
T4
T5
Response (a.u.)
Time (s)
F1
F0
R=0.91
R=0.99
R=0.93
R=0.96
R=0.93
R=0.92
R=0.98
R=0.63
R=0.97
R=0.99
R=0.99
R=0.99
R=0.99
R=0.91
R=0.99
BG contrast
0
8%
16%
32%
64%
100%

Figure S4 | Raw calcium responses for basic contrast stimuli. Related to Figure 3.
(**A**) Shown is only a subset of the data evaluated in Figure 3. Background contrast of 0 % is indicated by black lines, background contrast of 100 % is depicted in magenta. Responses are shown only for 3 out of 7 foreground contrasts. (**B–P**) Average calcium responses of all neurons to combinations of different foreground and background contrasts. (**Q**) Shown is a correlation analysis of the same dataset as in Figure 3 for the lamina cells L1–L5. On the y-axis is the F1-component of the calcium response (as evaluated in Figure 3) while the x-axis indicates the F0-component of the signal, i.e. the average calcium response during the stimulus. Data points corresponding to the same BG contrast are connected by lines and color-coded analogously to Figure 3. All data points are normalized to the maximum F1 response for each cell type. The gray dashed line marks the diagonal of the coordinate system. Correlation coefficient R is indicated in each panel. (**R**) Same as in Q but for ON-pathway medulla cells Mi1–Mi9 and for T4 cells. (**S**) Same as in Q but for OFF-pathway medulla cells Tm1–Tm9 and for T5 cells. (**T**) Color legend for panels Q–S. Darker color shade corresponds to higher background contrast, similarly to Figure 3. Zero background contrast condition is shown in black. See Table S2.

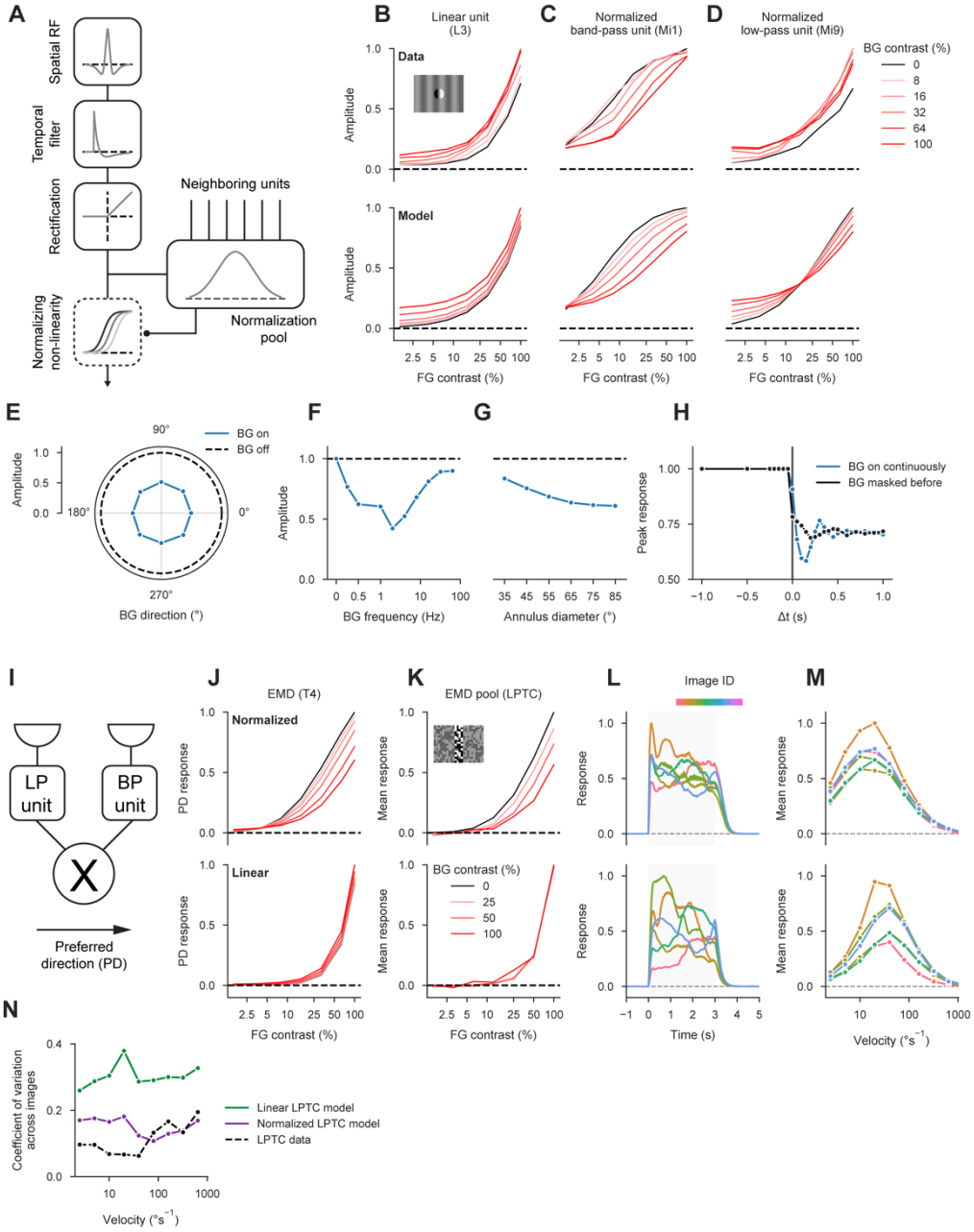

Figure S5 | Data-driven functional model of normalization circuit. Related to Figure 4. (**A**) Illustration of signal cascade for data-driven cell model (STAR Methods). Filter elements are sketched for an ON band-pass cell with normalization. (**B–D**) Contrast tuning curves for three model cells, estimated using the same protocol as during calcium imaging (FG = foreground, BG = background). Top, empirical data for L3, Mi1, and Mi9 (see Figure 3). Inset depicts a single frame from stimulus centered on recorded cell with background contrast 25 % and foreground contrast 100 %. Bottom, tuning curves from models manually tuned to resemble their empirical counterparts (see STAR Methods for parameters). (**E**) Responses of normalized ON band-pass cell model to orientation tuning stimulus (see Figure 4A; dashed line marks reference stimulus without background). Stimuli and evaluation were exactly matched to the experiment. (**F**) Responses of the same model to background frequency tuning experiment (see Figure 4B; dashed line marks reference stimulus without background). (**G**) Responses of the same model to background size stimulus (see Figure 4C;

dashed line marks reference stimulus without background). (**H**) Responses of the same model to contrast-step protocol (see Figure 4D). (**I**) Illustration of T4 or T5 model. Signals from a strongly normalized band-pass and a weakly normalized low-pass unit covering adjacent areas of the visual field are multiplied, yielding a direction-selective signal. (**J–M**) Top, responses from motion detector models with normalization. Bottom, responses from motion detector models in which normalization was switched off for both input arms. (**J**) Foreground contrast tuning for simulated T4 cell (see Figure 3). (**K**) Responses to behavioral contrast stimulus for a LPTC model composed of T4 and T5 models (STAR Methods). (**L**) Responses to various natural scenes moving at 20 $^{o}s^{-1}$ (modelled and evaluated as in Figure 1). (**M**) Velocity tuning curves for natural scenes (modelled and evaluated as in Figure 1). (**N**) Coefficient of variation across images for individual image velocities (derived from velocity tuning curves in M and Figure 1F; STAR Methods). A model including input normalization outperformed the linear model and approximated the variability of LPTC responses.

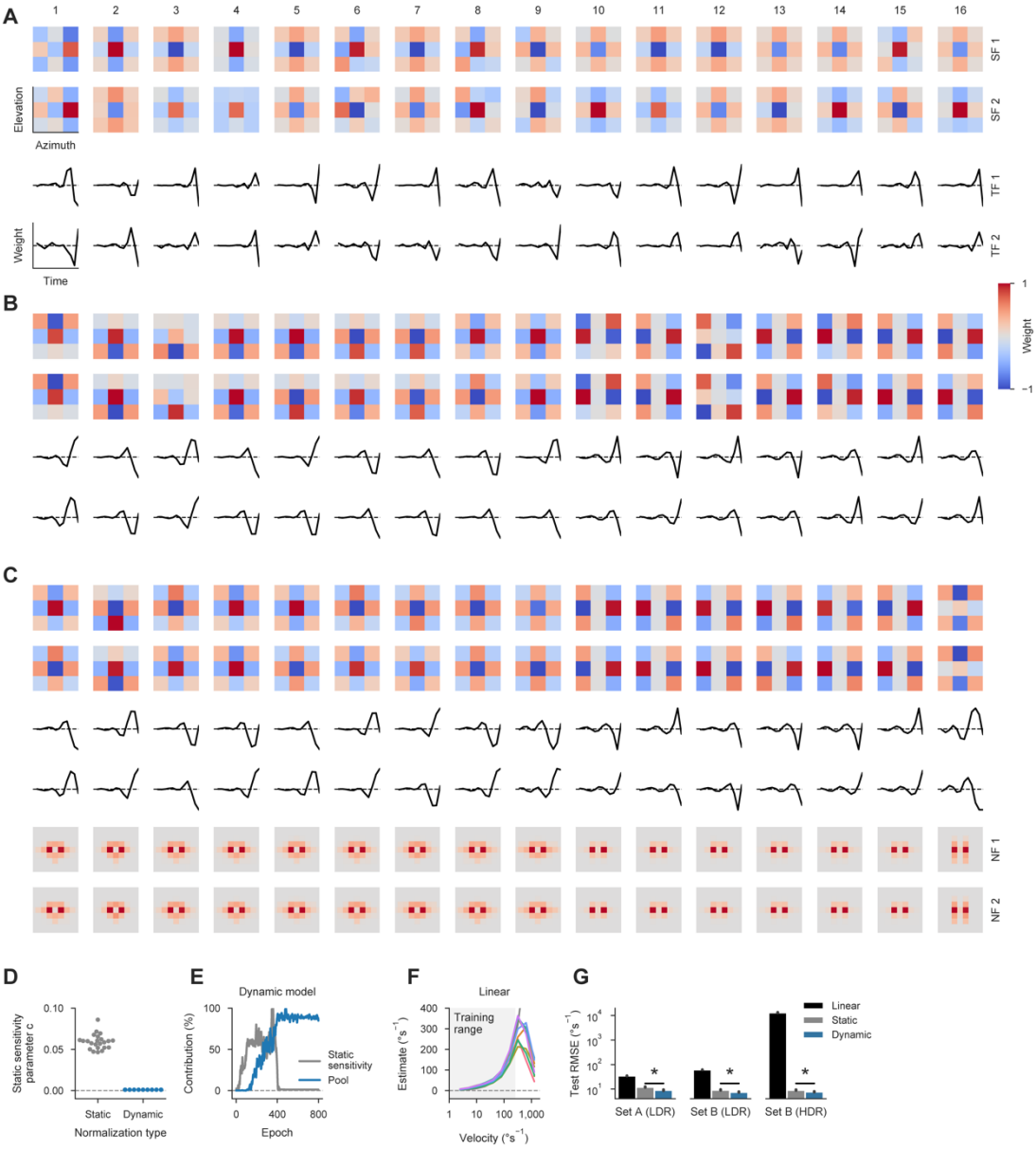

Figure S6 | Detailed receptive fields and performance data for task-driven model. Related to Figure 6.

(**A–C**) Receptive fields and temporal filters for 16 models of each non-linearity configuration (A, linear; B, static; C, dynamic). Models were sorted by test set error (increasing from left to right). Each pair of spatial and temporal filters was normalized to the maximum absolute weight across both channels (SF = spatial filter, TF = temporal filter, NF = normalization filter). Axis limits are the same as in Figure 6. (**D**) Values of sensitivity parameter *c* for all static (N=23) and dynamic (N=16) normalization models. (**E**) Evolution of weights for a single dynamic model. Both curves were independently normalized to their maximum across epochs. Pool contribution was quantified as the sum of weights across both 11 x 11 x 1 normalization filters. (**F**) Velocity tuning curves of best-performing linear model for various images (analogously to Figure 6G). Gray curve indicates true scene velocity on logarithmic axis. (**G**) Quantification of average model performance for all tested data sets (analogously to Figure 6H; LDR = low dynamic range, HDR = high dynamic range). See STAR Methods for details on how data sets were generated. Note that performance is plotted on a logarithmic axis. N=22/23/16 for linear/static/dynamic; *P<0.001; t=9.01/7.51/7.72 for set A/set B (LDR)/set B (HDR); Student's t-test with assumed equal variance; only difference between static and dynamic was tested.

Cell type	L_{fg}	L_{bg}	p	c_{50}	w_{pool}	q	Norm. index	$R^2_{DivisiveNorm}$	R^2_{linear}
L1	1.47	0.07	1.10	0.53	0.22	0.97	0.42	98.39 ± 0.10	92.55 ± 0.14
L2	1.10	0.05	1.37	0.23	0.36	0.77	1.58	99.29 ± 0.03	85.17 ± 0.13
L3	1.68	0.16	1.46	1.00	0.00	1.27	0.00	95.90 ± 0.08	97.17 ± 0.07
L4	1.41	0.12	1.23	0.53	0.32	1.09	0.61	98.94 ± 0.04	93.71 ± 0.07
L5	1.04	0.05	1.29	0.14	0.19	1.10	1.36	94.51 ± 0.23	69.34 ± 0.24
Mi1	1.03	0.03	1.21	0.06	0.25	1.05	4.33	97.37 ± 0.14	56.26 ± 0.41
Mi4	1.61	0.33	0.90	1.00	0.31	5.92	0.31	90.08 ± 0.26	87.50 ± 0.35
Mi9	1.69	0.23	0.99	1.00	0.40	2.87	0.40	92.40 ± 0.24	89.61 ± 0.32
T4	0.96	0.01	2.47	0.11	0.49	0.74	4.45	96.78 ± 0.15	74.17 ± 0.35
T5	1.08	0.07	1.97	0.26	1.17	0.92	4.55	97.02 ± 0.13	77.27 ± 0.27
Tm1	0.98	0.09	1.87	0.18	0.86	0.71	4.75	97.53 ± 0.11	78.67 ± 0.29
Tm2	1.08	0.17	1.36	0.20	1.14	0.91	5.76	97.58 ± 0.08	73.09 ± 0.32
Tm3	1.02	0.01	1.97	0.16	0.53	0.72	3.39	97.97 ± 0.12	82.33 ± 0.20
Tm4	1.06	0.11	2.33	0.40	1.44	0.81	3.61	96.77 ± 0.16	76.96 ± 0.37
Tm9	1.83	0.50	0.92	0.98	1.01	1.65	1.03	96.37 ± 0.14	87.42 ± 0.25

Table S1 | Fits for divisive normalization model. Related to Figure 3.

Short name	Full genotype	Used in
WT	w^+/w^+; +/+; +/+	Figure 1, Figure 2
T4/T5 block	w^+/w^-; R59E08-AD/UAS-TNT; R42F06-DBD/+	Figure S2
L1-GCaMP6f	w^+/w^-; VT027316-AD/UAS-GCaMP6f; R40F12-DBD/UAS-GCaMP6f	Figure 3, Figure S3–S4
L2-GCaMP6f	w^+/w^-; R53G02-AD/UAS-GCaMP6f; R29G11-DBD/UAS-GCaMP6f	Figure 3, Figure S3–S4
L3-GCaMP6f	w^+/w^-; R59A05-AD/UAS-GCaMP6f; R75H07-DBD/UAS-GCaMP6f	Figure 3, Figure S3–S4
L4-GCaMP6f	w^+/w^-; R20A03-AD/UAS-GCaMP6f; R31C06-DBD/UAS-GCaMP6f	Figure 3, Figure S3–S4
L5-GCaMP6f	w^+/w^-; R21A05-AD/UAS-GCaMP6f; R31H09-DBD/UAS-GCaMP6f	Figure 3, Figure S3–S4
Mi1-GCaMP6f	w^+/w^-; R19F01-AD/UAS-GCaMP6f; R71D01-DBD/UAS-GCaMP6f	Figure 3, Figure 4, Figure S4
Tm3-GCaMP6f	w^+/w^-; R13E12-AD/UAS-GCaMP6f; R59C10-DBD/UAS-GCaMP6f	Figure 3, Figure 4, Figure S4
Mi4-GCaMP6f	w^+/w^-; R48A07-AD/UAS-GCaMP6f; R13F11-DBD/UAS-GCaMP6f	Figure 3, Figure S4
Mi9-GCaMP6f	w^+/w^-; R48A07-AD/UAS-GCaMP6f; VT046779-DBD/UAS-GCaMP6f	Figure 3, Figure S4
Tm1-GCaMP6f	w^+/w^-; R41G07-AD/UAS-GCaMP6f; R74G01-DBD/UAS-GCaMP6f	Figure 3, Figure 4, Figure S4
Tm2-GCaMP6f	w^+/w^-; +/UAS-GCaMP6f; VT012282/UAS-GCaMP6f	Figure 3, Figure 4a-c, Figure S4
Tm2split-GCaMP6f	w^+/w^-; R28D05-AD/UAS-GCaMP6f; R82F12-DBD/UAS-GCaMP6f	Figure 4
Tm4-GCaMP6f	w^+/w^-; +/UAS-GCaMP6f; R35H01/UAS-GCaMP6f	Figure 3, Figure S4
Tm9-GCaMP6f	w^+/w^-; +/UAS-GCaMP6f; VT065303/UAS-GCaMP6f	Figure 3, Figure S4
T4-GCaMP6f	w^+/w^-; VT016255-AD/UAS-GCaMP6f; VT012314-DBD/UAS-GCaMP6f	Figure 3, Figure S3, Figure S4
T5-GCaMP6f	w^+/w^-; VT013975-AD/UAS-GCaMP6f; R42H07-DBD/UAS-GCaMP6f	Figure 3, Figure S3, Figure S4
Mi1-GCaMP6f, TNT-E	w^+/w^-; R19F01-AD/UAS-TNT-E; R71D01-DBD/UAS-GCaMP6f	Figure 5
Mi1-GCaMP6f, TNTin	w^+/w^-; R19F01-AD/UAS-TNTin; R71D01-DBD/UAS-GCaMP6f	Figure 5

Tm3-GCaMP6f, TNT-E	w^+/w^-; R13E12-AD/UAS-TNT-E; R59C10-DBD/UAS-GCaMP6f	Figure 5
Tm3-GCaMP6f, TNTin	w^+/w^-; R13E12-AD/UAS-TNTin; R59C10-DBD/UAS-GCaMP6f	Figure 5
Tm1-GCaMP6f, TNT-E	w^+/w^-; R41G07-AD/UAS-TNT-E; R74G01-DBD/UAS-GCaMP6f	Figure 5
Tm1-GCaMP6f, TNTin	w^+/w^-; R41G07-AD/UAS-TNTin; R74G01-DBD/UAS-GCaMP6f	Figure 5
Tm2split-GCaMP6f, TNT-E	w^+/w^-; R28D05-AD/UAS-TNT-E; R82F12-DBD/UAS-GCaMP6f	Figure 5
Tm2split-GCaMP6f, TNTin	w^+/w^-; R28D05-AD/UAS-TNTin; R82F12-DBD/UAS-GCaMP6f	Figure 5

Table S2 | Genotypes and abbreviations. Related to Figures 1–5.

Supplemental Reference

S1. Arenz, A., Drews, M.S., Richter, F.G., Ammer, G., and Borst, A. (2017). The temporal tuning of the *Drosophila* motion detectors is determined by the dynamics of their input elements. Curr. Biol. 27, 929–944.